Inorganic Chemistry

Article

pubs.acs.org/IC

[M(*rac*-*N*-benzyl Asp)(H_2O)] (M = Co, Ni): Noncentrosymmetric Coordination Polymeric Chains with Racemic Chiral Ligands

Junghwan Do,*[,†] Yumi Lee,[†] Jaeun Kang,[†] Yong Sun Park,[†] Bernd Lorenz,[‡,§] and Allan J. Jacobson*[,⊥]

[†]Department of Chemistry, Konkuk University, Seoul 143-701, Republic of Korea

[‡]Texas Center for Superconductivity, University of Houston, Houston, Texas 77204-5002, United States

[§]Department of Physics, University of Houston, Houston, Texas 77204-5005, United States

[⊥]Department of Chemistry, University of Houston, Houston, Texas 77204-5641, United States

Supporting Information

ABSTRACT: The hydrothermal reaction of fumaric acid, benzylamine, and metal salts yielded M[(*rac*-*N*-benzyl-Asp)(H_2O)] (M = Co, Ni), **1** and **2**, and Ni[(*rac*-*N*-benzyl-Asp)(H_2O)$_3$]·H_2O **3**. Under mild hydrothermal conditions, Michael addition of benzylamine to fumaric acid led to the formation of a racemic mixture of *N*-benzyl aspartic acid enantiomers. The noncentrosymmetric structures of **1** and **2** consist of one-dimensional polymeric chains in which metal cations are bridged by D- and L-*N*-benzyl aspartate anions alternating along the chain. The centrosymmetric structure of **3** is composed of discrete Ni[(*rac*-*N*-benzyl-Asp)(H_2O)$_3$] units that are connected by hydrogen bonds into layers. The single layers are homochiral but are hydrogen bonded to similar homochiral layers that contain the *N*-benzyl aspartate with the opposite handedness. Compounds **1** and **2** showed second harmonic generation (SHG), and their magnetic and thermodynamic properties are described.

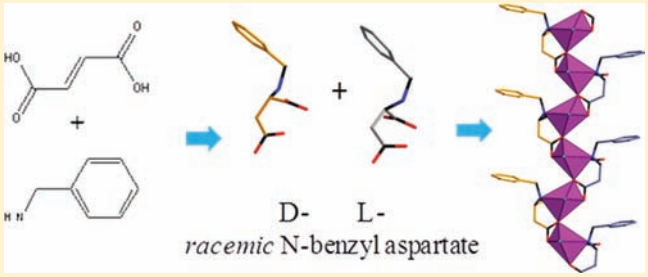

INTRODUCTION

Recently, metal−organic coordination polymers with noncentrosymmetric (acentric) structures have received significant attention due to their potential applications in second-order nonlinear optics (NLO), ferroelectrics, piezoelectrics, and pyroelectrics.[1,2] In general, noncentrosymmetric materials can be rationally designed by using preferred coordination geometries of metal centers and/or carefully chosen bridging ligands.[2] Several strategies have been developed to synthesize coordination polymers with noncentrosymmetric or chiral structures. The use of optically pure chiral multidentate ligands has proved to be the most effective and straightforward approach.[3−6] A racemic mixture of chiral ligands often results in crystallization of a true racemate with equal amounts of L- and D-enantiomers ordered in a way that leads to a centrosymmetric space group. In a few cases, however, crystals are formed that contain both ligand enantiomers, but in a noncentrosymmetric space group.[6−8] Examples of this class include Cd(L-N_3)$_2$(H_2O)$_2$ (L = trans-2,3-dihydro-2-(4′-pyridyl)-3-(3″-cyanophenyl)benzo[*e*]indole and [Cd(papa)(Hpapa)]ClO_4·$6H_2O$ (Hpapa = 3-(3-pyridyl)-3-aminopropionic acid).[8] In these structures, many weak interactions, such as H-bonds and $\pi-\pi$ stacking, are responsible for preventing the cancellation of the dipoles.

Here, we report the synthesis, structures, and magnetic and thermodynamic properties of M[(*rac*-*N*-benzyl-Asp)(H_2O)] (M = Co, Ni; *rac* = racemate), **1** and **2**, which are, to our knowledge, the first examples of a noncentrosymmetric coordination polymer structure containing a racemic ligand with one chiral center (monochiral). Racemic *N*-benzyl aspartic acid was formed by Michael addition of benzylamine to fumaric acid under mild hydrothermal conditions. A structurally related discrete molecule, Ni[(*rac*-*N*-benzyl-Asp)-(H_2O)$_3$]·H_2O, **3** is also described.

EXPERIMENTAL SECTION

Materials and Measurements. All chemicals used during this work were of reagent grade and used as received from commercial sources without further purification. Powder X-ray diffraction analyses were performed using a PANalytical X'Pert PRO diffractometer (Cu Kα radiation). Thermogravimetric analyses (TGA) were carried out in air at a heating rate of 2 °C/min, using a high-resolution TGA 2950 thermogravimetric analyzer (TA Instruments). Infrared spectra were recorded on a Hartmann & Braun BOMEM FTIR spectrometer within a range of 400−4000 cm^{-1} using the KBr pellet method. Qualitative analyses of the compounds were performed with a JEOL JSM-5200 scanning electron microscope (SEM) equipped with an EDAX Genesis energy-dispersive spectroscopy (EDS) detector. UV−visible reflectance data were collected on a Varian Cary 500 scan UV−vis-NIR spectrophotometer over the 200−1500 nm spectral range at room temperature. The absorption spectrum of the sample was approximated using the Kubelka−Munk function: $\alpha/S = (1 - R)^2/2R$, where R is the reflectance at a given wavelength, α is the absorption coefficient, and S is the scattering coefficient. Poly(tetrafluoroethylene) was used as a reference material. Powder SHG measurements were performed on a modified Kurtz-NLO

Received: October 24, 2011
Published: February 24, 2012

   dx.doi.org/10.1021/ic202302x | *Inorg. Chem.* 2012, 51, 3533−3539

system using a pulsed Nd:YAG laser with a wavelength of 1064 nm. Converse piezoelectric measurements were performed on samples pressed into 12 mm diameter, ~1 mm thick pellets. The pellets were cold isostatically pressed at 3500 psi at room temperature and then heated to 200 °C for 1 day. Silver paste was applied to both sides of the pellets. The polarization was measured on a Radiant Technologies RT66A Ferroelectric Test System with a TREK high-voltage amplifier between room temperature and 165 °C in a Delta 9023 environmental test chamber. Elemental analyses were performed at Galbraith Laboratories, Knoxville, TN. The magnetic properties were measured in a magnetic properties measurement system (MPMS, Quantum Design) at temperatures between 2 K and ambient as well as in magnetic fields up to 50 kOe. The specific heat was studied using a relaxation method in a commercial Physical Property Measurement System (PPMS, Quantum Design).

Synthesis. *Co[(rac-N-benzyl-Asp)(H_2O)] (**1**).* Hydrothermal reactions were carried out in 23 mL capacity Teflon-lined stainless steel Parr hydrothermal reaction vessels at 180 °C for 3 days. Cobalt acetate (0.130 g, 1.0 mmol), fumaric acid (0.116 g, 1.0 mmol), benzylamine (0.33 mL, 3.0 mmol), and H_2O (5 mL) were allowed to react. The solution pH values before and after the reaction were ~8 and ~5, respectively. The product was filtered, and red platy crystals were found as a single phase. The yield of the product, **1**, was 56%, based on cobalt. The product is stable in air and water and insoluble in common solvents, such as ethanol, DMF, acetone, and THF. EDS analysis confirmed the presence of Co. The elemental analyses gave the following results: obsd. (wt %) (Co, 19.4; C, 44.2; N, 4.58; H, 4.48), calcd (wt %) (Co, 19.7; C, 44.2; N, 4.68; H, 4.68). IR (KBr): 3366 m(br), 3195 s, 2959 w, 2923 w, 1653 s, 1541 s, 1445 m, 1400 m, 1351 w, 1339 w, 1311 w, 1227 w, 1109 w, 1071 w, 1033 w, 997 w, 970 w, 893 w, 877 w, 813 w, 752 w, 736 w, 700 m, 637 w, 599 w, 560 w cm^{-1}.

*Synthesis of Ni[(rac-N-benzyl-Asp)(H_2O)] (**2**).* Hydrothermal reactions were carried out in 23 mL capacity Teflon-lined stainless steel Parr hydrothermal reaction vessels at 200 °C for 3 days. Nickel chloride hexahydrate (0.130 g, 1.0 mmol), fumaric acid (0.116 g, 1.0 mmol), benzylamine (0.33 mL, 3.0 mmol), and H_2O (5 mL) were allowed to react. The solution pH values before and after the reaction were ~9. The product was filtered, and greenish blue platy crystals were found as a single phase. The yield of the product, **2**, was 65%, based on nickel. The product is stable in air and water and insoluble in common solvents, such as ethanol, DMF, acetone, and THF. EDS analysis confirmed the presence of Ni. The elemental analyses gave the following results: obsd. (wt %) (Ni, 20.2; C, 44.3; N, 4.71; H, 4.51), calcd (wt %) (Ni, 19.6; C, 44.2; N, 4.69; H, 4.69). IR (KBr): 3376 m(br), 3194 s, 3028 w, 2929 w, 1704 m, 1655 s, 1552 s, 1494 w, 1452 w, 1439 w, 1400 m, 1354 w, 1311 w, 1227 w, 1167 w, 1124 w, 1099 w, 1076 w, 1029 w, 1004 w, 974 w, 894 w, 879 w, 815 w, 742 w, 700 m, 603 w, 562 w cm^{-1}.

*Synthesis of Ni[(rac-N-benzyl-Asp)(H_2O)$_3$]·H_2O (**3**).* Hydrothermal reactions were carried out in 23 mL capacity Teflon-lined stainless steel Parr hydrothermal reaction vessels at 120 °C for 3 days. Nickel chloride hexahydrate (0.130 g, 1.0 mmol), fumaric acid (0.116 g, 1.0 mmol), benzylamine (0.11 mL, 1.0 mmol), and H_2O (5 mL) were allowed to react. The solution pH values before and after the reaction were ~7 and ~4, respectively. The product was filtered, and pale blue, thin rod-shaped crystals were found as a single phase. The yield of the product, **3** was 40%, based on nickel. The product is stable in air and water and insoluble in common solvents, such as ethanol, DMF, acetone, and THF. EDS analysis confirmed the presence of Ni. IR (KBr): 3406 s(br), 3199 s, 1635 s, 1562 s, 1495 w, 1429 m, 1403 m, 1333 w, 1309 w, 1220 w, 1122 w, 1097 w, 1069 w, 1009 w, 978 w, 890 w, 746 m, 696 m, 632 w, 600 w, 556 w cm^{-1}.

Single-Crystal Structure Determination. X-ray single-crystal analyses for **1**–**3** were performed on a Siemens SMART platform diffractometer outfitted with an Apex II area detector and monochromatized graphite Mo Kα radiation. The structures were solved by direct methods and refined using SHELXTL.[9] The hydrogen atoms of the *N*-benzyl aspartate were generated geometrically and allowed to ride on their respective parent atoms. The hydrogen atoms of the coordinated water molecules for **1** and **2** were found by difference Fourier analysis and refined isotropically; the hydrogen atoms of coordinated and lattice water molecules for **3** were not located. All non-hydrogen atoms were refined anisotropically. The Flack parameter refined to 0.04(3) and 0.01(2) for **1** and **2**, respectively. Both compounds **1** and **2** are SHG-active (see below), confirming that they are noncentrosymmetric. Crystal data for compounds **1**, **2**, and **3** are summarized in Table 1. CCDC reference nos. 783740, 783741, and 783742 are for **1**, **2**, and **3**, respectively. The data for **1**–**3** can be obtained free of charge from the Cambridge Crystallographic Data Centre via www.ccdc.cam.ac.uk/data_request/cif.

Table 1. Crystallographic Data for 1–3

	1	2	3
empirical formula	$C_{11}H_{13}CoNO_5$	$C_{11}H_{13}NNiO5$	$C_{11}H_{19}NNiO_8$
formula wt	298.15	297.9	351.99
temperature, K	296(2)	296(2)	296(2)
cryst syst	monoclinic	monoclinic	monoclinic
space group	*Pn*	*Pn*	$P2_1/n$
a, Å	5.9522(8)	5.9343(4)	8.238(2)
b, Å	13.3808(17)	13.2243(10)	6.0097(15)
c, Å	7.9745(10)	7.9584(6)	30.584(8)
β, deg	110.252(2)	110.410(1)	92.298(4)
V, $Å^3$	595.87(13)	585.34(7)	1513.0(7)
Z	2	2	4
D_c, g cm^{-3}	1.662	1.690	1.550
μ, mm^{-1}	1.452	1.670	1.319
GOF on F^2	1.076	1.084	0.861
R1 ($I > 2\sigma(I)$)	0.0339	0.0282	0.0489
wR2 (all data)	0.0904	0.0742	0.1339

RESULTS AND DISCUSSION

Crystal Structures. We found that the Michael addition of benzylamine to fumaric acid takes place smoothly under mild hydrothermal reaction conditions. The direct amination of the unsaturated dicarboxylic acid produced *N*-benzyl aspartic acid during the reaction with a metal salt (nickel chloride hexahydrate or cobalt acetate) and water. Although several synthetic methods for amination of α,β-unsaturated dicarboxylic acid derivatives, such as mono- or diester and monoamide, are well-known, the direct amination of α,β-unsaturated dicarboxylic acid has been rarely reported.[10]

Compounds **1** and **2** are isostructural, and only the structure of **1** will be described. One crystallographically distinct cobalt atom is coordinated by one nitrogen and two oxygen atoms from an *N*-benzyl aspartate group. Two additional oxygen atoms from a second *N*-benzyl aspartate unit and one water molecule complete the distorted octahedral geometry with the Co–O distances in the range of 2.056(3)–2.242(3) Å; the Co–N distance is 2.124(3) Å (Figure 1). The $CoO_4N(H_2O)$ octahedron is severely distorted from the regular 90° angles (59.8(1)–112.8(1)°) and 180° angles (161.35(7)–169.5(1)°) due to the steric requirement of the chelating carboxylate group (Figure 1). One nitrogen and three out of four oxygen atoms (O1, O2, O3) in *N*-benzyl aspartate groups are coordinated to cobalt atoms, and one remaining oxygen atom (O4) in a carboxylate group is terminal. Cobalt atoms are bridged by O2 atoms to form ···Co–O2–Co–O2··· chains with the alternating distances of 2.081(3) and 2.242(3) Å in the [101] direction, forming the infinite neutral chain, Co[(*rac*-*N*-benzyl-Asp)(H_2O)] (Figure 2). A novel feature of this asymmetric chain is the arrangement of D- and L-*N*-benzyl

dx.doi.org/10.1021/ic202302x | *Inorg. Chem.* 2012, 51, 3533–3539

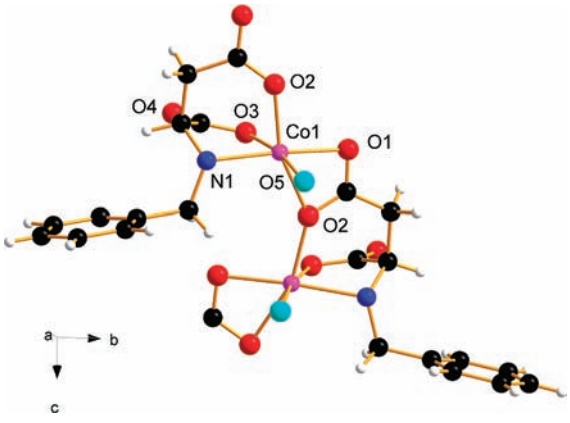

Figure 1. View of the local structure of **1**. Carbon, oxygen, nitrogen, hydrogen, oxygen (H_2O), and Co atoms are shown as black, red, blue, white, light blue, and pink spheres, respectively.

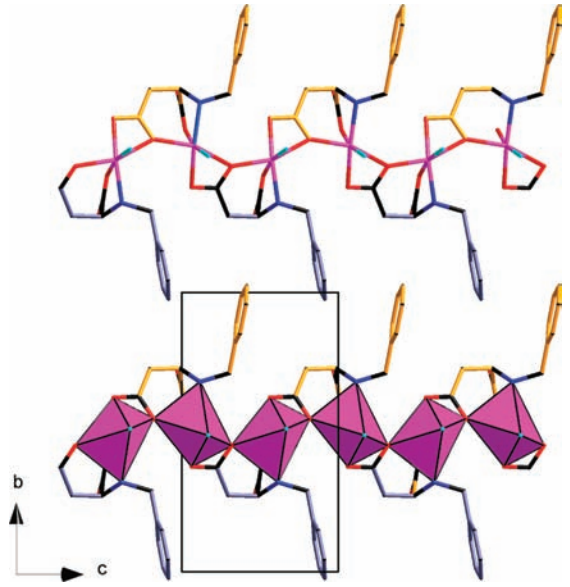

Figure 2. View of **1** showing the interchain packing on the *bc* plane. Pink circles and polyhedra represent Co atoms, and the other labeling scheme is the same as that in Figure 1, except that gold and gray bonds are used to highlight the arrangement of the two enantiomers of the *N*-benzyl aspartate ions.

aspartate groups that are coordinated to cobalt atoms on the left and right side of each chain, respectively.

Adjacent chains are arranged so that the benzyl groups are interdigitated. The interchain distance between the benzyl groups is >3.76 Å, suggesting that van der Waals interactions predominate with only weak $\pi-\pi$ stacking along the chain direction. The weak interactions along the *c* axis are reflected in the high thermal displacement parameters of the carbon atoms in the benzyl group (Figure 3). The structure is further stabilized by the presence of hydrogen bonds between the coordinated water molecules and the carboxylate oxygen atoms [$O5_W\cdots O3$ = 2.752(1) and 2.856(1) Å] in adjacent chains, which results in the formation of layers on the *ac* plane (Figures 4 and 5).

The structure of **3** is built up of discrete Ni[(*N*-benzyl-Asp)-$(H_2O)_3$] molecules packed with lattice water molecules (Figure 6). Compound **3** contains the same racemic *N*-benzyl aspartate anions as are found in **1** and **2**. One crystallographically unique nickel

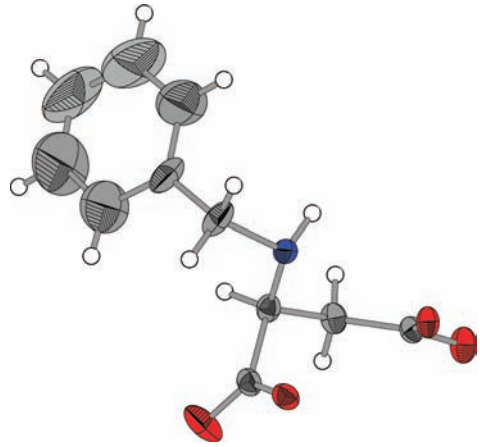

Figure 3. Displacement ellipsoids of non-hydrogen atoms in the *N*-benzyl aspartate unit in **1** drawn at the 50% probability level. Carbon, oxygen, and nitrogen atoms are gray, red, and blue ellipses, respectively. Hydrogen atoms are represented by white spheres.

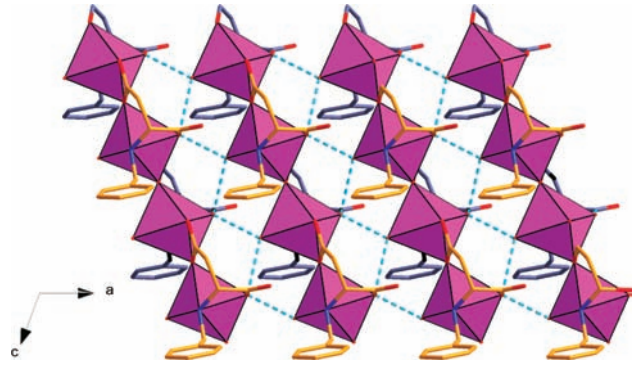

Figure 4. Layers formed in the *ac* plane in **1** by hydrogen bonding (dotted blue lines) between the chains and the stacking of the layers along *b*. Colors are as shown in Figure 2.

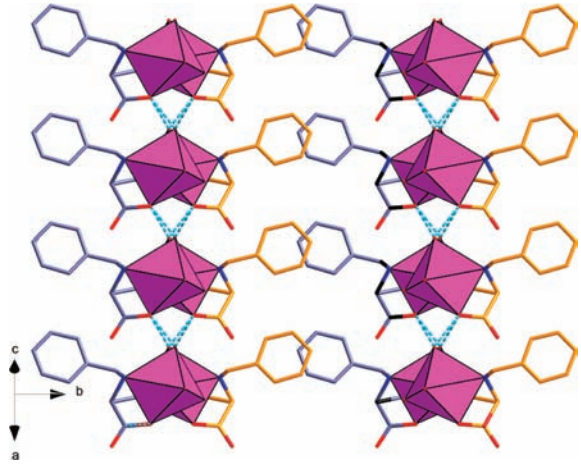

Figure 5. Layers formed in the *ac* plane in **1** by hydrogen bonding (dotted blue lines) between the chains and the stacking of the layers along *b*.

atom is coordinated by one nitrogen atom and two oxygen atoms from a single *N*-benzyl aspartate and three water molecules to form an octahedron with Ni−O, Ni−N, and Ni−OH_2 with distances of 2.036(3), 2.058(3), 2.088(3), 2.058(3), 2.078(3),

dx.doi.org/10.1021/ic202302x | *Inorg. Chem.* 2012, 51, 3533−3539

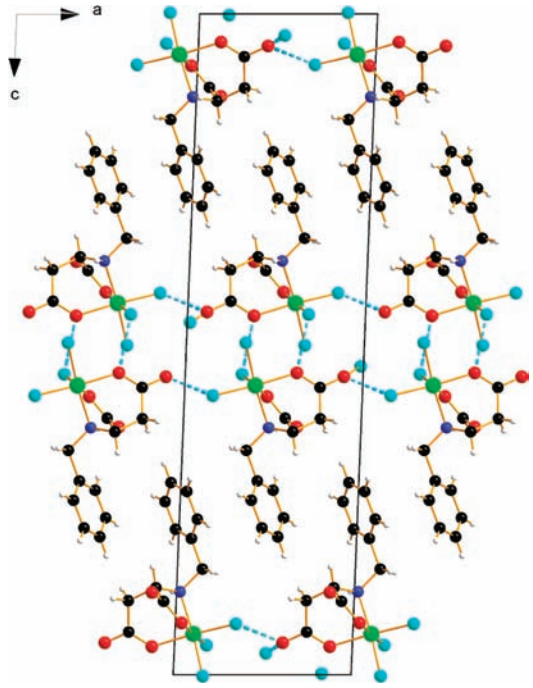

Figure 6. Structure of **3** viewed along *b*. Carbon, oxygen, nitrogen, hydrogen, oxygen (H_2O), and Ni atoms are shown as black, red, blue, white, light blue, and green spheres, respectively. Hydrogen bonds are shown as dotted blue lines.

and 2.085(3) Å, respectively. The $NiO_2N(H_2O)_3$ octahedron is slightly distorted from ideal 90° angles (81.8(1)−96.3(1)°) and 180° angles (172.3(2)−178.1(1)°). Unlike **1** and **2**, the *N*-benzyl aspartate carboxylate groups do not chelate, and consequently, the $NiO_2N(H_2O)_3$ octahedron is not severely distorted.

The structure of **3** contains an extended network of O−H···O hydrogen bonds (Figure 6). The coordinated water molecules are H-bonded to adjacent oxygen atoms in the carboxylate groups. Lattice water molecules are also hydrogen bonded to oxygen atoms in the carboxylate groups. Single layers of Ni[(*N*-benzyl-Asp)$(H_2O)_3$] molecules are formed in the *ab* plane through hydrogen bonds. The single layers are homochiral but are hydrogen bonded to similar homochiral layers that contain the *N*-benzyl asparate with the opposite handedness, forming double layers (Figure 6). The double layers stack along the *c* axis and interact through van der Waals forces between the projecting benzyl groups.

Characterization. Thermogravimetric analysis in air shows that **1** remains stable up to ∼250 °C (Figure S1, Supporting Information). On further heating, a weight loss of 72.50% occurs near 300 °C in a single step. The final product after heating was identified as Co_3O_4 by powder X-ray diffraction. The overall observed weight loss is in good agreement with that calculated for the formation of Co_3O_4 (73.16%). The thermal decomposition behavior of **2** (Figure S2, Supporting Information) is very similar to that of **1**. Thermogravimetric analysis in air shows that **2** remains stable up to ∼250 °C. On further heating, a weight loss of 74.32% occurs near 300 °C at a single step. The final product after heating treatment was identified as NiO by powder X-ray diffraction, and the overall observed weight loss is in good agreement with that calculated for the formation of NiO (75.00%). The decomposition behavior of compound **3** was investigated because it seemed possible that **2** might form from **3** on dehydration as the structure of the molecular units are closely related (Figure S3, Supporting Information). The lattice water molecules are lost immediately in flowing air and completely by 80 °C, making it difficult to establish an accurate overall weight loss. Two of the coordinated water molecules are lost in two well-defined steps that are complete by 150 and 200 °C. The compound then decomposes to form NiO, beginning at ∼280 °C and complete by 320 °C, as found for compound **2**. Between 200 and 280 °C, the composition of **3** is the same as that of **2**. High-temperature X-ray diffraction measurements in this temperature range did not indicate the formation of crystalline **2** from the thermal decomposition of **3**.

The solid-state UV−vis spectra of **1** and **2** were determined (Figures S4 and S5, Supporting Information). Compound **1** shows one weak absorption band at 8900 cm^{-1}, assigned to $^4T_{1g}(F) \rightarrow {}^4T_{2g}(F)$ and the other strong multiplet band in the region of 19 000−22 000 cm^{-1} assigned to $^4T_{1g}(F) \rightarrow {}^4T_{1g}(P)$. Between the major two bands, a very weak band is observed at 16 100 cm^{-1}, assigned to $^4T_{1g}(F) \rightarrow {}^4A_{2g}(F)$. The observed d−d transitions are expected for octahedrally coordinated Co(II). The red color of the crystal **1** is due to the absorption of light at 526 nm (∼19 000 cm^{-1}), corresponding to the complementary color of green. Compound **1** is an insulating material with a band gap at room temperature of 4.5 eV. The major UV bands for **2** occur at 9950, 15 500, and 26 000 cm^{-1}. These are associated with the d−d spin-allowed transitions for octahedral Ni^{2+} from the $^3A_{2g}$ ground state to the three excited triplet terms. The spin-allowed transitions are assigned to transitions to the $^3T_{2g}$, $^3T_{1g}(F)$, and $^3T_{1g}(P)$ states, respectively. The shoulder at ∼13 300 cm^{-1} is the result of the spin-forbidden transition to the ^1E_g term. The results of **2** are comparable to the values for aqueous solutions of Ni^{2+}.[11] The greenish blue color of the crystal **2** is due to the absorption of light at 9950 cm^{-1} (645 nm), corresponding to the complementary color of orange. Compound **2** is an insulating material with a band gap at room temperature of 4.3 eV.

Compounds **1** and **2** are SHG (second harmonic generation)-active, and powder SHG measurements for **1** and **2** showed a comparable efficiency to ∼ α-SiO_2. No piezoelectric or polarization properties could be observed for **1** using 12 mm diameter, 1 mm thick pellets.

Magnetic Properties. The magnetic susceptibility $\chi(T)$ of **1** measured at 1000 Oe is shown in Figure 7a. A magnetic phase transition is observed at 5 K, and the sharp peak in $\chi(T)$ suggests that the magnetic order is antiferromagnetic in **1**. The AFM nature of the transition is further supported by the field dependence of the magnetization (Figure 8a). Below 5 K, in the AFM state, a metamagnetic transition similar to a spin-flop transition is observed with increasing external field, resulting in a steplike increase of the magnetization (inset of Figure 8a). At higher fields, $\boldsymbol{M}(\boldsymbol{H})$ increases smoothly, but it does not saturate at 50 kOe, the maximum field of this investigation. The magnetization value of about 0.7 μ_B at 50 kOe is significantly smaller than that expected for the Co^{2+} with a spin of 3/2.

In contrast, the magnetic order of **2** shows a weak ferromagnetic (FM) moment below T_C = 18 K. The susceptibility of **2** measured at a low field of 10 Oe is shown in Figure 7b. The difference between field cooling (FC) and zero field cooling (ZFC) of $\chi(T)$ (Figure 7b) and the $\boldsymbol{M}(\boldsymbol{H})$ data shown in Figure 8b with a hysteresis loop at lower fields (inset) provide evidence for the existence of a weak FM moment. However, the FM moment is very small and the coercive field at 2 K is only 1200 Oe. At higher magnetic fields, $\boldsymbol{M}(\boldsymbol{H})$ increases almost linearly with $\boldsymbol{H}$ up to 50 kOe, with a magnetization value at 50 kOe,

dx.doi.org/10.1021/ic202302x | *Inorg. Chem.* 2012, 51, 3533−3539

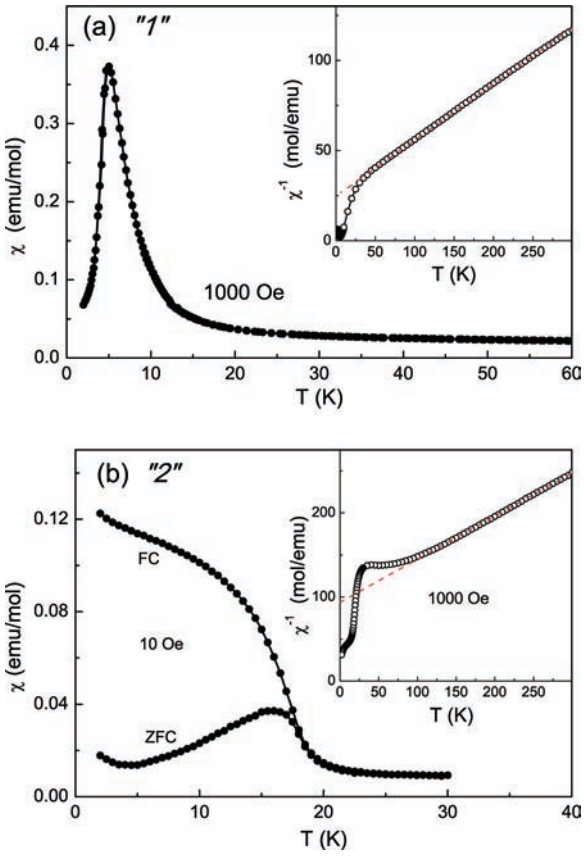

Figure 7. (a) Magnetic susceptibility of **1** showing the antiferromagnetic transition at T_N = 5 K. The inset shows the inverse susceptibility and the linear Curie–Weiss dependence at higher temperatures. (b) Magnetic susceptibility of **2** revealing the ferromagnetic transition at T_C = 18 K. Inset: inverse susceptibility and Curie–Weiss extrapolation. The Curie–Weiss parameters are discussed in the text.

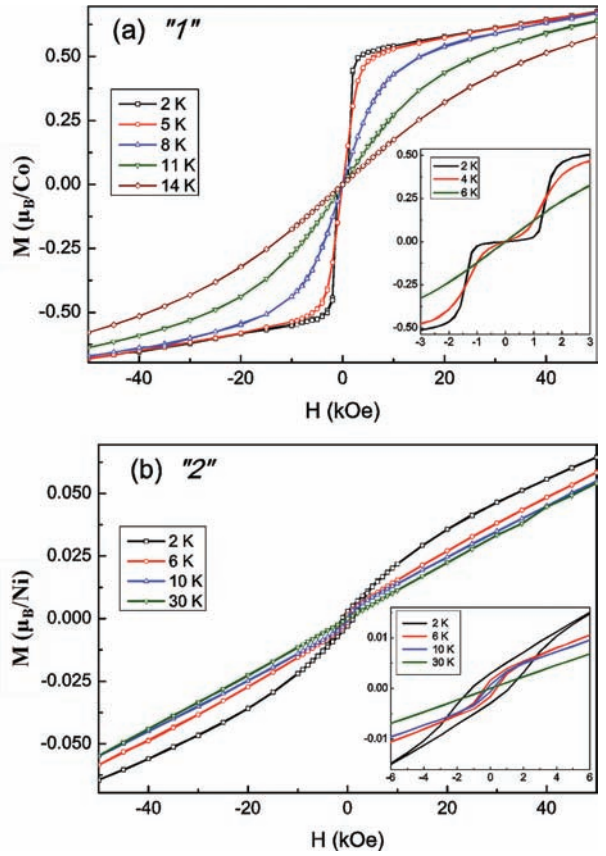

Figure 8. Magnetization vs field of the antiferromagnet **1** (a) and the ferromagnet **2** (b) at selected temperatures. The inset of (a) shows the magnetization details of **1** at low fields with a metamagnetic (spin-flop) transition in the ordered state. The low-field data shown in the inset of (b) confirm the weak ferromagnetic character (***M*–*H*** hysteresis loops) of the low-temperature phase of **2**.

which is even an order of magnitude smaller than that of the Co compound **1**.

The ***M***(***H***) data of Figure 8 and the low magnetic moments at 50 kOe show that the magnetic exchange interactions between nearest-neighbor transition-metal ions in **1** and **2** are strong and AFM in nature. According to the structure discussed above, the nearest transition-metal ions form quasi one-dimensional chains with an oxygen ion (O2) linking two transition metals. The dominant magnetic interactions along the chain are, therefore, superexchange interactions. With an angle of M–O2–M slightly less than 180°, those interactions are antiferromagnetic according to the Goodenough–Kanamori rules.[12] Therefore, strong AFM correlations can be expected among Co or Ni ions within the chains.

The AFM nature of the spin–spin correlations is further supported by the high-temperature magnetization data of **1** and **2**, shown in the insets to Figure 7. The inverse susceptibilities of both samples follow the Curie–Weiss law at high temperatures and the relevant parameters, Curie–Weiss temperature θ_{CW} and effective magnetic moment μ_{eff}, are derived from the linear part of $1/\chi$. For **1**, we obtain θ_{CW} = −80 K and μ_{eff} = 5.0 μ_B. The negative θ_{CW} proves the dominant AFM interactions within the chains. The nearest-neighbor exchange interaction constant J can be estimated from the mean field formula $\theta_{CW} = zJ/k_B$. With z = 2 in the chain structure, we get $J/k_B \approx 40$ K. The large effective moment of 5 μ_B confirms the high-spin state of the Co^{2+}, exceeding even the spin-only value of 3.87 μ_B, which is expected for S = 3/2. This can be explained by an incomplete quenching of the orbital momentum as reported for various compounds with high-spin Co^{2+} before.[13] For **2**, the Curie–Weiss parameters are θ_{CW} = −184 K ($J/k_B \approx 92$ K) and μ_{eff} = 3.9 μ_B. The AFM intrachain exchange coupling of the Ni spins is about twice as strong as the coupling of the Co spins.

Magnetic long-range order, however, cannot be established in purely one-dimensional systems. The interchain magnetic coupling is needed to stabilize an ordered state. Those interchain exchange interactions are very weak because of the large distance between the magnetic ions of neighboring chains and the weak interchain (van der Waals) forces. The interchain magnetic coupling could arise from magnetic dipolar interactions; however, the microscopic nature of the magnetic correlations has yet to be explored. The low transition temperatures (T_N = 5 K for **1**, T_C = 18 K for **2**) are consistent with a weak coupling of neighboring chains. The results of the magnetic measurements indicate that the ordered state in **1** is antiferromagnetic and it can be understood as an ordering of the AFM chains in three dimensions. The small ferromagnetic moment of **2** could be due to a slight canting of the Ni spins, giving rise to an FM ground state. Whether the canting exists already at higher temperatures or it arises at the ferromagnetic T_C is not clear, and other explanations, such as a small ferromagnetic moment, may be considered also. Local probes of the magnetic structure may shed more light onto the details of the magnetic order and fluctuations.

dx.doi.org/10.1021/ic202302x | *Inorg. Chem.* 2012, 51, 3533–3539

Specific Heat. The conclusions from magnetic measurements are supported by the results of a specific heat study at low temperatures. The specific heat for **1** and **2** is shown as C_p/T in Figure 9. The AFM transition of **1** is clearly indicated by a peak of C_p/T at T_N, which is shown in more detail on an expanded scale in the inset of Figure 9. However, this peak is

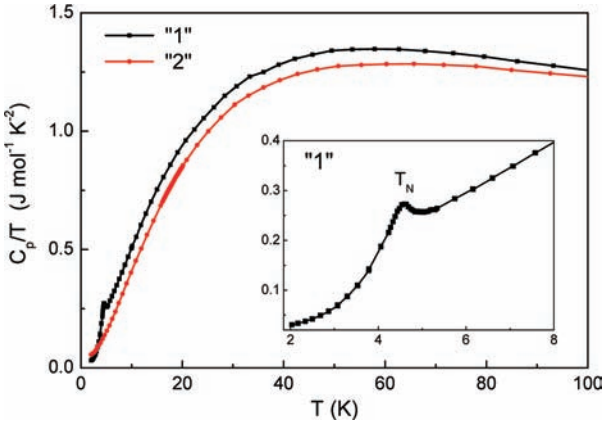

Figure 9. Heat capacity of **1** (squares) and **2** (circles) below 100 K. The inset shows the peak at the AFM transition of **1** at an enlarged scale.

relatively small in size and the entropy change associated with the AFM transition, as derived by integrating the peak area of the C_p/T data, is only $\Delta S \approx 0.06$ J/(mol K). This is a tiny fraction of the maximum entropy change for a spin 3/2 system from an ordered to a completely disordered state, $\Delta S_{max} = 11.5$ J/(mol K). The small entropy change across T_N proves the high degree of remaining spin order, supposedly along the chains, that survives to much higher temperatures, in accordance with the conclusions from magnetic measurements.

The ferromagnetic transition of **2** is even weaker, and no peak-like anomaly of the specific heat is detected near the FM transition temperature (Figure 9). The small change of the magnetization, though clearly visible in the magnetic data of Figure 8b, is apparently associated only with a minute change of entropy beyond the resolution of the specific heat measurements. These results lend further support to the conjecture that the FM order of **2** possibly results from a small canting of spins with an existing strong AFM short-range correlation.

CONCLUSION

Noncentrosymmetric coordination polymers, **1** and **2**, with chain structures are prepared by reaction of Co^{2+} and Ni^{2+} with *N*-benzyl aspartic acid. The ligand is formed under mild hydrothermal conditions in situ by Michael addition of benzylamine to fumaric acid. Compounds **1** and **2**, to our knowledge, are the first examples of noncentrosymmetric 1D coordination polymers formed from a racemic mixture of enantiomer with one chiral center. The structures of the chains show ordering of the enantiomers along the chains probably due to the steric requirements of the ligand, which results in highly efficient interchain packing. The asymmetric chain may be caused by the combined effects of steric hindrance of the ligand and H-bonding. The structure of **3** contains discrete molecules of $Ni[(rac\text{-}N\text{-benzyl-Asp})(H_2O)_3]$, which are connected to form layers via H-bonding and van der Waals' interactions. Both compounds, **1** and **2**, exhibit magnetic long-range order at low temperatures, which is antiferromagnetic for **1** and ferromagnetic for **2**. From magnetization and specific heat measurements, we conclude that the primary magnetic fluctuations are antiferromagnetic along the spin chains and they persist up to high temperatures. The long-range magnetic order for both compounds is weak and is a result of the weak interactions between neighboring chains. Compounds **1** and **2** are second harmonic generation (SHG)-active with efficiencies comparable to $\sim \alpha$-SiO_2. The d−d transitions of Ni and Co lower the transparency of the crystals, and so to improve the SHG properties, we are currently investigating compounds formed by optically transparent metals, such as Zn and Cd.[14] Also, we are studying various other ligands formed by Michael addition of donor−acceptor substituted conjugated amines to fumaric acid utilizing in situ hydrothermal reactions.

ASSOCIATED CONTENT

Supporting Information

Crystallographic data (CIF) for **1**−**3**, TGA data for **1**−**3**, and solid-state emission spectra for **1** and **2**. This material is available free of charge via the Internet at http://pubs.acs.org.

AUTHOR INFORMATION

Corresponding Author

*E-mail: junghwan@konkuk.ac.kr (J.D.), ajjacob@uh.edu (A.J.J.). Tel: +82-2-450-3416 (J.D.), 713-743-2785 (A.J.J.). Fax: 82-2-3436-5382 (J.D.), 713-743-2787 (A.J.J.).

Notes

The authors declare no competing financial interest.

ACKNOWLEDGMENTS

This work was supported by the National Research Foundation of Korea Grant funded by the Korean Government (KRF-2008-314-C00190), the Robert A. Welch Foundation (Grant No. E0024), and the Texas Center for Superconductivity at the University of Houston.

REFERENCES

(1) (a) Zhang, G.; Yao, S.-Y.; Guo, D.-W.; Tian, Y.-Q. *Cryst. Growth Des.* **2010**, *10*, 2355−2359. (b) Fu, D.-W.; Zhang, W.; Xiong, R.-G. *Dalton Trans.* **2008**, 3946−3948. (c) Evans, O. R.; Xiong, R.-G.; Wang, Z.; Wong, G. K.; Lin, W. *Angew. Chem., Int. Ed.* **1999**, *38*, 536−538. (d) Guo, Z. G.; Cao, R.; Wang, X.; Li, H. F.; Yuan, W. B.; Wang, G. J.; Wu, H. H.; Li, J. *J. Am. Chem. Soc.* **2009**, *131*, 6894. (e) Zhang, W.; Ye, H.-Y.; Xiong, R.-G. *Coord. Chem. Rev.* **2009**, *253*, 2980−2997 and references therein.

(2) (a) Evans, O. R.; Lin, W. *Acc. Chem. Res.* **2002**, *35*, 511−522. (b) Ayyapan, P.; Evans, O. R.; Cui, Y.; Wheeler, K. A.; Lin, W. B. *Inorg. Chem.* **2002**, *41*, 4978. (c) Shi, L. L.; Liao, Y.; Yang, G. C.; Su, Z. M.; Zhao, S. S. *Inorg. Chem.* **2008**, *47*, 2347. (d) Zhang, L.; Qin, Y. Y.; Li, Z. J.; Lin, Q. P.; Cheng, J. K.; Zhang, J.; Yao, Y. G. *Inorg. Chem.* **2008**, *47*, 8286. (e) Xue, D. X.; Zhang, W. X.; Chen, X. M.; Wang, H. Z. *Chem. Commun.* **2008**, 1551.

(3) (a) Ye, Q.; Wang, S.-X.; Zhao, H.; Xiong, R.-G. *Chem. Soc. Rev.* **2005**, *34*, 208. (b) Zhang, W.; Xoing, R.-G.; Huang, S. D. *J. Am. Chem. Soc.* **2008**, *130*, 10468. (c) Zhao, H.; Ye, Q.; Qu, Z.-R.; Fu, D.-W.; Xiong, R.-G.; Huang, S. D.; Chan, W. P. H. *Chem.—Eur. J.* **2008**, *14*, 1164. (d) Ye, Q.; Song, Y.-M.; Wang, G.-X.; Chen, K.; Fu, D.-W.; Chan, P. W.-H.; Zhu, J.-S.; Huang, D. S.-P.; Xiong, R.-G. *J. Am. Chem. Soc.* **2006**, *128*, 6554.

(4) (a) Eerenstein, W.; Mathur, N. D.; Scott, J. F. *Nature* **2006**, *442*, 759. (b) Jain, P.; Dalal, N. S.; Toby, B. H.; Kroto, H. W.; Cheetham, A. K. *J. Am. Chem. Soc.* **2008**, *130*, 10450. (c) Ye, Q.; Hang, T.; Fu, D.-W.; Xu, G.-H.; Xiong, R.-G. *Cryst. Growth Des.* **2008**, *8*, 3501. (d) Ohkoshi, S.; Tokoro, H.; Matsuda, T.; Takahashi, H.; Irie, H.; Hashimoto, K. *Angew. Chem., Int. Ed.* **2007**, *46*, 3238. (e) Cui, H. B.;

Wang, Z. M.; Takahashi, K.; Okano, Y.; Kobayashi, H.; Kobayashi, A. *J. Am. Chem. Soc.* **2006**, *128*, 15074. (f) Okubo, T.; Kawajiri, R.; Mitani, T.; Shimoda, T. *J. Am. Chem. Soc.* **2005**, *127*, 17598.
(5) (a) Evans, C.; Luneau, D. *Dalton Trans.* **2002**, 83−86. (b) Lou, B.; Jiang, F.; Yuan, D.; Wu, B.; Hong, M. *Eur. J. Inorg. Chem.* **2005**, 3214−3216.
(6) Anokhina, E. V.; Jacobson, A. J. *J. Am. Chem. Soc.* **2004**, *126*, 3044−3045.
(7) Brock, C. P.; Schweizer, W. B.; Dunitz, J. D. *J. Am. Chem. Soc.* **1991**, *113*, 9811.
(8) (a) Ye, Q.; Tang, Y.-Z.; Wang, X.-S.; Xiong, R.-G. *Dalton Trans.* **2005**, 1570−1573. (b) Qu, Z.-R.; Zhao, H.; Wang, Y.-P.; Wang, X.-S.; Ye, Q.; Li, Y.-H.; Xoing, R.-G.; Abrahams, B. F.; Liu, Z.-G.; Xue, Z.-L.; You, X.-Z. *Chem.—Eur. J.* **2004**, *10*, 53−60.
(9) Sheldrick, G. M. *SHELXTL: Program for Refinement of Crystal Structures*; Siemens Analytical X-ray Instruments: Madison, WI, 1994.
(10) Piispanen, P. S.; Pihko, P. M. *Tetrahedron Lett.* **2005**, *46*, 2751−2755 and references therein.
(11) Figgis, B. N.; Hitchman, M. A. *Ligand Field Theory and Its Applications*; King, R. B., Ed.; Wiley-VCH: New York, 2000; Chapter 8, pp 204−210.
(12) (a) Goodenough, J. B. *Phys. Rev.* **1955**, *100*, 564−573. (b) Goodenough, J. B. *J. Phys. Chem. Solids* **1958**, *6*, 287−297. (c) Kanamori, J. *J. Phys. Chem. Solids* **1959**, *10*, 87−98.
(13) (a) Hossain, M. J.; Sakiyama, H. *Inorg. Chim. Acta* **2002**, *338*, 255−259. (b) Viola, M. C.; Martinez-Lope, M. J.; Alonso, J. A.; Martinez, J. L.; De Paoli, J. M.; Pagola, S.; Pedregosa, J. C.; Fernandez-Diaz, M. T.; Carbonio, R. E. *Chem. Mater.* **2003**, *15*, 1655−1663. (c) Tong, M.-L.; Ru, J.; Wu, Y.-M.; Chen, X.-M.; Chang, H.-C.; Mochizuki, K.; Kitagawa, S. *New J. Chem.* **2003**, *27*, 779−782.
(14) (a) Evans, C.; Luneau, D. *Dalton Trans.* **2002**, 83−86. (b) Lacroix, P. G.; Di Bella, S.; Ledoux, I. *Chem. Mater.* **1996**, *8*, 541−545.